Fabrication of self-supporting structures made of washcoat materials (γ-Al₂O₃-CeO₂) by ceramic stereolithography: Towards digital manufacturing of enhanced catalytic converters

Setareh Zakeri [a,*], Teemu Vastamäki [a], Mari Honkanen [b], Matti Järveläinen [a], Minnamari Vippola [a,b], Erkki Levänen [a]

[a] Materials Science and Environmental Engineering, Faculty of Engineering and Natural Sciences, Tampere University (TAU), Tampere, Finland
[b] Tampere Microscopy Center, Tampere University (TAU), Tampere, Finland

HIGHLIGHTS

- A novel fabrication method for catalytic converters using stereolithography is proposed.
- A resin made of washcoat materials (γ-Al₂O₃-CeO₂) is printed into self-supporting structures.
- The addition of CeO₂ to the plain γ-Al₂O₃ resin significantly reduces the curing depth.
- Microstructure characterizations show hierarchical porosity of the printed structures.
- Surface area measurements show that CeO₂ stabilized the printed γ-Al₂O₃ at 1100 °C, not 900 °C.

GRAPHICAL ABSTRACT
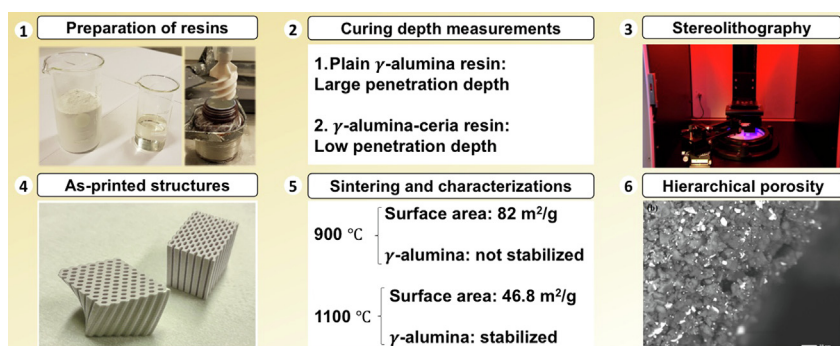
ABSTRACT

Despite increasing interest in the use of alternative fuel, conventional diesel or gasoline powered vehicles still dominate road transportation; removal of their emitted pollutants is a challenge to sustainable transportation. The automotive industry has employed catalytic converters (CCs) to effectively modify or eliminate toxic pollutants emitted by combustion engines. The efficiency of a CC greatly depends on its geometry and is hindered by limitations in fabrication techniques. To go beyond these limits and further enhance the performance of CCs, one can use state-of-the-art ceramic stereolithography (CSL) technology, which enables fabrication of complex-shaped structures. In this work, a novel photocurable ceramic resin made of γ-Al₂O₃ and CeO₂ (the commonly used washcoat materials in CCs) is shaped into the honeycomb and twisted honeycomb structures using CSL. Measurements reveal that upon the addition of CeO₂ to the plain γ-Al₂O₃ resin, the penetration depth of light is significantly decreased from 408.06 μm to 75.19 μm. This research also focuses on the balance between having a high surface area and achieving good physical stability in the printed structures. Accordingly, the appropriately debinded structures are sintered at two different temperatures: 900 °C and 1100 °C. It is found that the structure sintered at 900 °C has a higher surface area, and thus, it is a better candidate for catalytic applications. Furthermore, investigation of the stabilizing effect of CeO₂ on printed γ-Al₂O₃ finds that CeO₂ is effective in stabilizing the printed γ-Al₂O₃ at 1100 °C but not 900 °C. Targeting the realization of green and sustainable transportation, the applied CSL technique in this study enables flexible control in the design and

* Corresponding author.
    E-mail address: setareh.zakeri@tuni.fi (S. Zakeri).

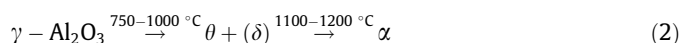fabrication of self-supporting structures that are expected to open promising ways for the optimization of CCs.

1. Introduction

Since the global community began to address the increasing levels of hazardous air pollutants and enacted stringent emission regulations, catalytic converters (CCs) have become a commercial solution that reduce the serious environmental impacts of automotive exhaust emissions [1]. A CC is a device that converts car exhaust emissions, including carbon monoxide (CO), hydrocarbons (HC), and nitrogen oxides (NO_x), into less toxic or even harmless inert products through catalytic reactions [1,2]. Installed between the engine and tailpipe, CCs typically consist of (i) a substrate (ceramic or metal honeycomb structure), (ii) a washcoat layer, and (iii) active catalysts (often a mix of precious metals) [2,3]. The substrate has high physical stability and a low thermal expansion coefficient to resist cracking or thermal shocks during the rapid temperature transients which happen during driving cycles. However, the surface area of the substrate is quite low, resulting in limited dispersion of the active catalysts on its surface. Thus, a thin layer (10–150 μm) of a porous ceramic material with a high surface area, known as washcoat, is washcoated on the interior walls of the substrate [4]. The washcoat layer acts as a host by providing more sites for dispersion of the active catalysts, which are later added to the structure by impregnation. The pollutants diffuse within the waschoat and react on the active catalyst sites [5]. Fig. 1 shows a schematic of a conventional CC.

Because washcoat materials are added to allow efficient mass transport and good catalytic performance, they must have desirable characteristics, such as high surface area, suitable pore size distribution, and high thermal stability. γ-Al_2O_3, has been the universal choice as the main washcoat material in CCs, owing to its high porosity and surface area [6,7]. Alumina (Al_2O_3) exists in eight

different phases, seven of which are metastable (γ, δ, κ, ρ, η, θ, χ), and one of which is thermally stable (α). The metastable phases of alumina tend to transform into the α-phase at relatively high temperatures (1000–1200 °C) with the following transition sequences [8]:

$$\gamma - Al_2O_3 \xrightarrow{750\ °C} \delta \xrightarrow{900\ °C} \theta \xrightarrow{1200\ °C} \alpha \tag{1}$$

$$\gamma - Al_2O_3 \xrightarrow{750-1000\ °C} \theta + (\delta) \xrightarrow{1100-1200\ °C} \alpha \tag{2}$$

The phase transition from γ- to α-Al_2O_3 is accompanied by a drastic decrease in surface area and a volume reduction of about 10% [9,10]. For excellent performance of a CC, operating in hot exhaust emissions at high temperatures, it is required to prevent the thermal transformation of active γ-Al_2O_3 into inactive, low-surface-area, and less-porous α-Al_2O_3 [7,11]. Therefore, stabilizers such as ceria and lanthania are typically added to the washcoat to preserve the surface area of γ-Al_2O_3 [6]. Ceria (CeO_2) is known as a phase-stabilizing agent for γ-Al_2O_3, and it is commonly used in CCs because of its high oxygen storage capacity, which enhances some crucial intermediate reactions during catalysis [11,12]. Besides stabilizers, other additives such as zirconia, silica, and zeolite are typically added to the washcoat layer in smaller quantities for various purposes.

The conversion performance of a CC is remarkably relying on the space velocity of the exhaust gas, defined as the ratio of the volumetric flow rate (m^3s^{-1}) of the exhaust gas to the volume of the CC (m^3). The reciprocal of space velocity is residence time. The exhaust gases passing through the CC at high space velocities may not have enough residence time for the catalytic reactions, leading to reduced performance. In contrast, low space velocities yield better performance, but they may need the use of larger-sized CCs or low flow rates through the engine (affecting the engine performance). This clearly demonstrates that the performance of a CC depends not only on the chemistry of the washcoat but also on factors involved in system design, such as geometry, size, and position [13,14]. Due to the limitations of conventional methods in fabricating complex structures, the efficiency of CCs is hindered.

Additive manufacturing (AM) or 3D printing, is a highly integrated and versatile approach that employs a layer-by-layer or even pixel-by-pixel fabrication strategy based on a computer-aided design (CAD) model to build complex, freeform, and previously un-manufacturable geometries [15]. Owing to its easy preparation and the unique digital control over material shape, composition, size, and porosity, AM has been used in the fabrication of porous structures in the catalytic applications [16–22]. Among potential ceramic AM techniques, ceramic stereolithography (CSL) can fabricate high-quality structures with enhanced resolution and lower surface roughness. The CSL technique consolidates complicated structures out of a liquid resin by using light to successively cure thin layers of material on top of each other. The resin consists of acrylate and epoxide-based photoactive polymers, photoinitiators, and the ceramics in powder form, all dispersed homogeneously. The laser beam provides the required energy for photopolymerization in which monomers are bonded to each other and a highly cross-linked polymer is formed [23].

In this study, a novel photocurable ceramic resin made of γ-Al_2O_3 and CeO_2, with suitable rheological and photocuring char-
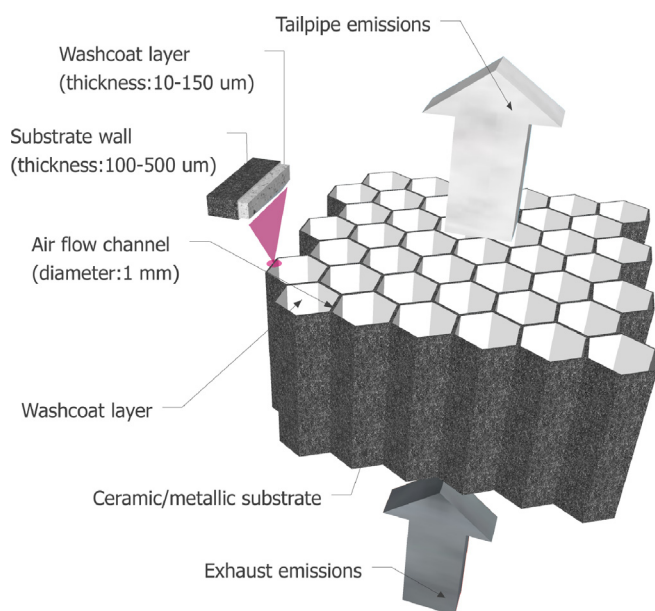

Fig. 1. Schematic of a conventional CC. Exhaust emissions (NO_x, CO, and HC) pass through the channels and react with the washcoat, which contains the active catalysts. CCs convert these harmful emissions into less harmful or even inert emissions (CO_2, HO_2, and N_2), exiting from the tailpipe.

acteristics, was stereolithographically shaped into self-supporting (substrate-less) hierarchical porous structures, which are aimed to be further used in catalytic applications. The novelty of the proposed approach is fourfold: (i) fabricating the CC structures directly from the washcoat materials, without substrate, simplifies the conventional fabrication methods; (ii) using CSL, it is possible to fabricate any complex geometries, such as twisted honeycomb structures, which increase the residence time of the exhaust emissions passing through the structure, resulting in better performance or allowing smaller-sized CCs; (iii) the whole volume of the fabricated structure takes part in gas conversion instead of only a thin layer; (iv) interconnected pores within the structure provide high external mass transfer, high turbulence, high convective heat transfer, and low pressure drop, all resulting in better performance. The aim of this paper is to demonstrate the first and second novelties by fabricating such structures as shown in Fig. 2. The third and fourth novelties will be investigated in our next research by coating the printed structures with precious metals and assessing their catalytic efficiency.

The proposed fabrication process is required to be optimized by determining a sintering temperature for the printed structures at which they maintain a high surface area as well as good physical stability. Stronger structures require sintering at higher temperatures. Nevertheless, this would result in a drastic decrease in surface area in the case of γ-Al$_2$O$_3$, which tends to transform into other alumina phases at high temperatures. This is why ceria was added to the structure as it is known that it can preserve the surface area at least in conventional methods; in this study, it is investigated whether the stabilizing effect of ceria on γ-Al$_2$O$_3$ works in 3D printing of the two powders as well. Accordingly, two different temperatures of 900 °C and 1100 °C were selected for sintering of the printed structures since these temperatures are critical in the transition sequences of γ-Al$_2$O$_3$. Various characterization techniques, analytical electron microscopy, Brunner-Emmett-Teller (BET) surface area analysis, X-ray diffraction (XRD), and dilatometric analysis, were applied to analyze the raw materials and microstructure at different stages of the study. It is worth mentioning that this paper demonstrates the 3D printing of structures made from only two washcoat materials and that the printing parameters can be adjusted according to the proper-

ties of the raw washcoat materials, resulting in the fabrication of self-supporting structures that can be potentially used as CCs. The successful printing of these structures was a demonstration of the capability and precision of CSL to fabricate components that may enhance the performance of CCs by providing new designed geometries and overcoming the limitations of traditional CCs.

2. Materials and methods

2.1. Materials

The micro-sized γ-Al$_2$O$_3$ powder (Puralox SBa 150, mean agglomerate size d$_{50}$: 2–6 μm, surface area:150 m^2 g^{-1}) and the nano-sized CeO$_2$ powder (d$_{50}$: 100 nm, surface area: 30 m^2 g^{-1}) used in this research were supplied by Sasol Germany GmbH and AEM China, respectively. A photocurable raw resin (a mixture of acrylate monomers) with a density of 0.987 g cm^{-3}, which was crafted and validated in our own laboratory, was used for the preparation of ceramic resins. Mostly, photocurable monomers do not produce reactive species to commence photopolymerization by themselves. Hence, photoinitiators (PIs) are added to resins to produce reactive species to attack the functional groups of monomers. When the functional group is broken down, adjacent monomer molecules form strong covalent bonds, and the liquid resin converts to a solid gel with various bulk characteristics. In this study, Camphorquinone (PI$_1$) and Ethyl 4- (dimethylamino) benzoate (PI$_2$), both purchased from Aldrich, were used to initiate the photopolymerization process. The stability and viscosity of the ceramic resins were controlled by the addition of the dispersant agent (DISPERBYK-180, BYK Additives & Instrument).

2.2. Characterization of the as-received powders

Both the as-received powders were sintered at 900 °C and 1100 °C with a heating rate of 2 °C min^{-1} from room temperature up to the sintering temperature, a dwell time of 2 h at the sintering temperature, and a cooling rate of 5 °C min^{-1} down to the room temperature. As-received and sintered powders were both characterized using different techniques. A high resolution (scanning) transmission electron microscope ((S) TEM) (F200 S/TEM, Jeol, Japan), operating at 200 kV, was used to characterize the shape and particle size of the powders. Samples were prepared by crushing the powder between two glass slides and then dispersed in ethanol. After that, a drop of powder dispersion was placed onto the TEM copper grid with holey carbon film, which was later allowed to dry. BET surface area (SA) of the powders were measured with a gas adsorption analyzer (Micromeritics 3Flex, USA). The crystalline phases were identified by X-ray diffraction (XRD) using a Panalytical Empyrean multipurpose X-ray diffractometer (PANalytical B. V., the Netherlands) with a Cu K$_\alpha$ radiation source ($\lambda = 0.15418$ nm) and a PIXcel 3D detector to measure the scattered intensities as a function of the scattering angle 2θ. The X-ray generator was powered at 45 kV and 40 mA. Experimental conditions included a 2θ range of 20 °- 80 ° with a step size of 0.02 °, a beam mask of 10 mm, and a nickel filter. Phase identification was performed using the Panalytical HighScore Plus software (version 3.0.5) with the database PDF-4+ of the International Centre for Diffraction Data (Database version 4.1065). Additionally, dilatometry analysis was carried out to analyze the sintering behavior of the γ-Al$_2$O$_3$ and CeO$_2$ powders using a dilatometer (DIL 402 Expedis, Netzsch, Germany). The heat treatment program used for dilatometer measurements under the nitrogen gas atmosphere was: a heating rate of 2 °C min^{-1} from ambient temperature up to 1100 °C, a dwell time of 2 h at 1100 °C, and a cooling rate of
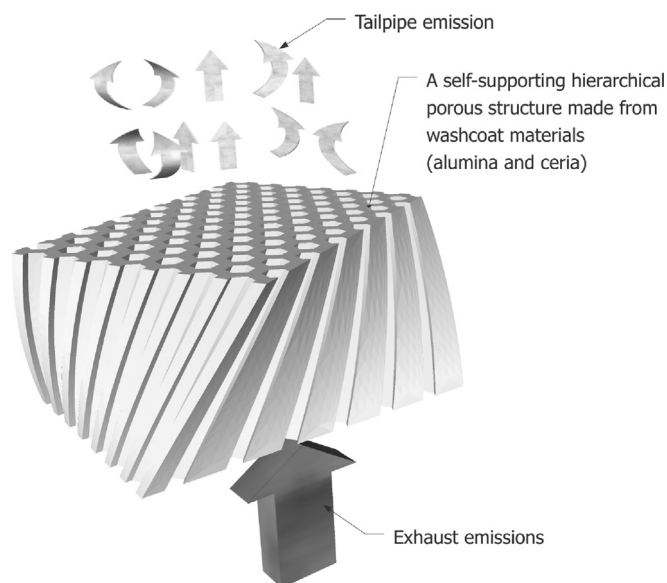

Fig. 2. Schematic of the proposed self-supporting hierarchical porous structure made from the washcoat materials (γ-Al$_2$O$_3$ and CeO$_2$).

5 °C min^{-1} down to the ambient temperature. Samples for dilatometry analysis were prepared by compressing 1 g of each powder, which was poured into a cylindrical die with a diameter of 19.5 mm, using a universal material testing machine (Instron 5967, Instron, USA) with a pressure of 100 MPa.

2.3. Preparation of the ceramic resins and viscosity measurements

The ceramic resins were prepared by mixing the raw photocurable resin with dispersant in a specific weight ratio. Then the ceramic powder was gradually added to the mixture, and afterward, the prepared ceramic resins were tumbler-milled with zirconia balls for 4 h. Chemical composition of the prepared ceramic resins with the specific amounts of γ-Al$_2$O$_3$, CeO$_2$, resin, and dispersant are summarized in Table 1. Once the ceramic powder was homogeneously mixed with the raw resin, PI$_1$ and PI$_2$ were added with the specific weight ratios (with respect to the raw resin) of 1 wt% and 2 wt%, respectively. Finally, the prepared photocurable ceramic resins were milled for an additional 1 h.

The viscosity of the prepared ceramic resins was measured by a stress-controlled rotational rheometer (Physica MCR-301, Anton Paar GmbH, Austria) at room temperature. Their rheological behavior was characterized by applying shear rates in the range of 1–1000 s^{-1}.

2.4. Photocuring behavior of the prepared ceramic resins and the printing process

The photocuring behavior of a ceramic resin can be characterized by measuring its two important parameters: penetration depth (D$_p$) and critical exposure energy (E$_c$). To this end, a thick layer of the prepared ceramic resins was irradiated by a blue LED emitter ($\lambda = 457$ nm, I $= 25.46$ mW cm^{-2}) for specific irradiation times (2–20 s) corresponding to different energy doses (E$_{max}$). For each exposure, the thickness of the cured layer, which is known as curing depth C$_d$, was then measured using a micrometer.The photocuring behavior of each ceramic resin was characterized by its associated working curve, which was obtained by plotting C$_d$ versus E$_{max}$ on a semi-log scale. The working curve is plotted according to the Beer-Lambert law, which describes the theoretical equation of the curing depth as follows [24]:

$$C_d = D_p \ \ln(E_{max}) - D_p \ \ln(E_c) \tag{3}$$

After extrapolation was conducted to fit the plotted curves, D$_p$ and E$_c$ were calculated.

Digital models of the desired structures were designed by Fusion 360 and exported as stereolithography files to the 3D printer. The promising ceramic resins, with appropriate rheological and photocuring behaviors, were then tested in the 3D printer (CeraFab 7500, Lithoz GmbH, Austria) with a layer thickness of 50 μm. To run the printing process, the exposure time (t) for the photopolymerization of a specific curing depth (250 μm) was calculated by the following equation [24]:

$$t = \frac{\exp(\frac{C_d}{D_p} + \ln(E_c))}{P} \tag{4}$$

where P is the power density of the light used in the printer.

A schematic illustration of the printing process of stereolithography sytems is shown in Fig. 3. After printing, the as-printed structures, which is a composite of polymer and ceramic, were rinsed to clean and remove the remaining uncured resin. The as-printed structures were thoroughly immersed in LithaSol20 (a special cleaning agent from Lithoz) followed by an ultrasonic bath for a duration of at least 10 min and were later flushed with 70% ethanol.

2.5. Debinding and sintering

To obtain a pure ceramic component in CSL, it is required that the as-printed structure be subjected to appropriate thermal treatment (debinding) for the removal of the cured polymer. To better understand the required heat treatment for the debinding process, thermogravimetric (TG) analysis was performed and studied on the carefully washed as-printed structures. TG analysis was carried out using a Netzsch thermo-microbalance apparatus (TG 209 F3 Tarsus, Netzsch, Germany) under nitrogen gas (99.99% purity) with a heating rate of 5 °C min^{-1} from room temperature up to 550 °C. Once a proper heat treatment program for the debinding process was obtained, the as-printed structures were debinded in a laboratory-scale muffle furnace (RHF1500, Carbolite, UK) under air atmosphere. Then, the debinded samples were sintered at 900 °C and 1100 °C because these temperatures are critical in the phase transformation of γ-alumina. The sintering time of the structures was 2 h since usually sintering times greater than this value result in pore growth with degraded properties. The same heat treatment program described in Section 2.2 was used for sintering the structures in a high-temperature furnace (ECF40/17, Entech, Sweden).

2.6. Characterizations of the printed structures

Microstructure characterizations of the as-printed and sintered structures were performed using a scanning electron microscope (SEM) (JSM-IT500LA, Jeol, Japan) as well as (S) TEM. Energy dispersive spectroscopy (EDS) was used to obtain comprehensive information on the elemental distribution of the printed structures through SEM-EDS (DrySD™ detector, Jeol, Japan) and STEM-EDS (Dual EDS system for F200, Jeol, Japan). Cross-sectional samples from the printed structures were prepared for SEM studies by placing the porous structures in liquid nitrogen for 1 min to avoid crushing them during the cutting process. The samples were then cut into pieces with a scalpel and fixed with the help of conductive carbon glue on a standard aluminum pin stub mount. The prepared porous samples were studied with SEM, in low vacuum mode (10 Pa) using a backscattered electron detector (BED) detector (BED-C), without any conductive coating. The SEM was operated at an accelerating voltage of 20 kV, and images were taken to investigate the homogeneity of the microstructure as well as the bonding between consecutive layers. To prepare samples for STEM, a piece of the sintered structure was crushed and then treated following the same procedures discussed in Section 2.2. The BET SA measurements and phase identifications through XRD patterns were also carried out for the printed structures (described in Section 2.2).

3. Results and discussion

3.1. Characterization of the as-received and sintered powders

In this study, it was aimed to use stereolithographically to fabricate structures with two oxide ceramics and sinter them at two
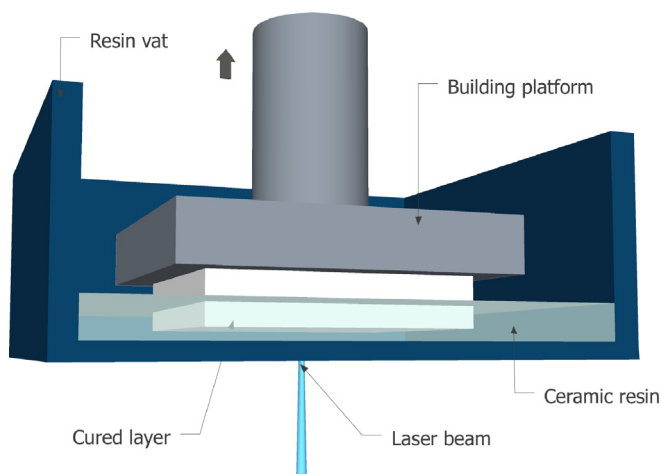
Table 1
Chemical components of the prepared ceramic resins used in this study and their concentrations.

Resin Name	γ-Al$_2$O$_3$ (vol%)	CeO$_2$ (vol%)	Resin (vol%)	Dispersant (wt%)
R$_1$	20	–	80	11
R$_2$	15	5	80	7

Fig. 3. Schematic illustration of the stereolithography system based on the bottom-up approach. The building platform on which the structure is built is immersed inside the resin vat, which has a transparent bottom. Laser exposure is performed from beneath the vat bottom. The cured layer is sandwiched between the previously cured layer and the vat bottom when exposed to laser. Each time a layer is cured, the building platform elevates to detach the cured layer from the vat bottom and allow the fresh resin to fill the region between the last cured layer and the vat bottom.

different temperatures. Alumina and ceria have different sintering behaviors, and ceria can partially stabilize alumina from phase transition which leads to a decrease in the surface area of alumina. Therefore, it is necessary to investigate each powder at each temperature individually. Both the as-received powders were sintered at 900 °C and 1100 °C. The as-received and sintered powders of alumina and ceria were characterized by the following techniques.

3.1.1. TEM characterization

The as-received powders of γ-Al$_2$O$_3$ and CeO$_2$ were observed by TEM. The TEM micrographs shown in Fig. 4 revealed information on the particle size as well as the morphology of the γ-Al$_2$O$_3$ and

CeO$_2$ powders. Fig. 4(a) shows that the as-received γ-Al$_2$O$_3$ powder consisted of needle-shaped primary particles that were stacked into agglomerates. By comparing the TEM images in Figs. 4(a) and 4(b), no significant variation was observed in the particle size and morphology of the as-received γ-Al$_2$O$_3$ powder when sintered at 900 °C. However, as shown in Fig. 4(c), the particle size was found to be remarkably increased once the alumina powder was sintered at 1100 °C. In addition, the influence of sintering temperature on the particle size of the as-received CeO$_2$ powder was studied and the results are presented in Figs. 4(d)-(f). Fig. 4(d) clearly shows that the as-received CeO$_2$ powder was composed of faceted primary particles. It was found that the particle size was considerably increased for both cases of sintering at 900 °C and 1100 °C (see Figs. 4(e) and 4(f)), indicating that sintering had already begun before 900 °C. Note that the length of the scale bar in Fig. 4(f) is 100 nm and twice the 50 nm scale bars in Figs. 4(d)-(e).

3.1.2. BET surface area measurement

Transition aluminas such as γ-phase are metastable without additives and tend to transform to the thermodynamically stable α-Al$_2$O$_3$ under heat treatment at higher temperatures. A drastic decrease in the surface area (SA) is assigned to the transition from γ- to α-Al$_2$O$_3$ [10]. As indicated in Table 2, the SA of the as-received γ-Al$_2$O$_3$ powder was slightly decreased from 150.40 m^2 g^{-1} to 124.00 m^2 g^{-1} when sintered at 900 °C. However, the associated SA was sharply decreased to 29.90 m^2 g^{-1} when sintered at 1100 °C, indicating the possible transition from γ- to α-Al$_2$O$_3$. Moreover, Table 2 shows that the SA of the as-received CeO$_2$ powder was noticeably decreased from 33.42 m^2 g^{-1} to 1.44 m^2 g^{-1} and 0.67 m^2 g^{-1} when sintered at 900 °C and 1100 °C, respectively. The measured SA obtained by BET analyses were in accordance with the TEM images in Fig. 4.

3.1.3. XRD analysis

To further investigate the effect of sintering temperature on the phase transition occurring during heat treatment of γ-Al$_2$O$_3$ and CeO$_2$ powders, XRD characterization was conducted. The measured XRD results for the as-received and sintered γ-Al$_2$O$_3$ powders are
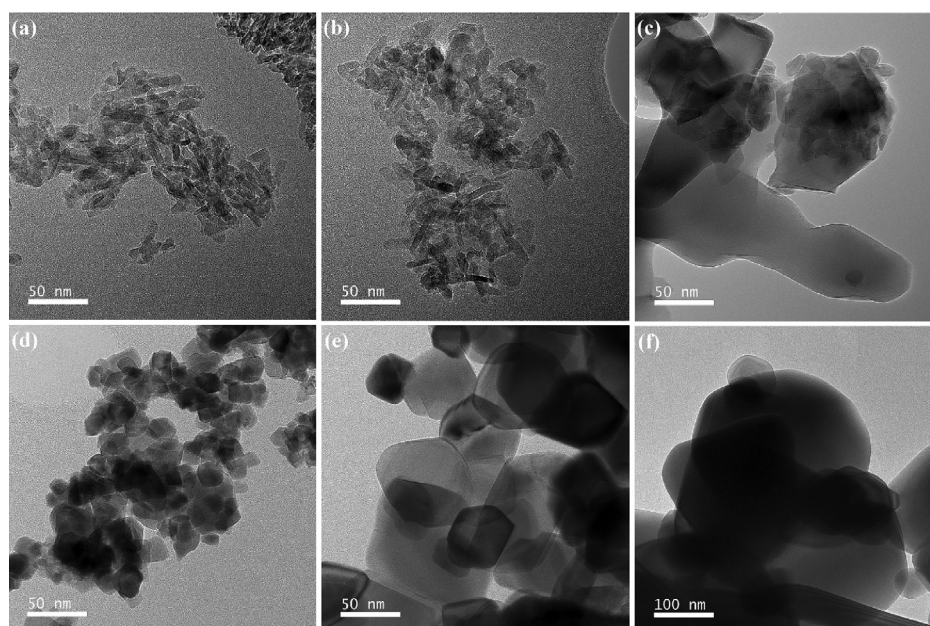

Fig. 4. High resolution TEM images of the as-received and sintered alumina and ceria powders. (a) as-received γ-Al$_2$O$_3$; (b) γ-Al$_2$O$_3$ sintered at 900 °C; (c) γ-Al$_2$O$_3$ sintered at 1100 °C; (d) as-received CeO$_2$; (e) CeO$_2$ sintered at 900 °C; (f) CeO$_2$ sintered at 1100 °C. The length of the scale bar in (f) is 100 nm and twice the 50 nm scale bars in (d) and (e).

Table 2
SA obtained by BET analyses associated with the as-received and sintered (at 900 °C and 1100 °C) powders of Al_2O_3 and CeO_2.

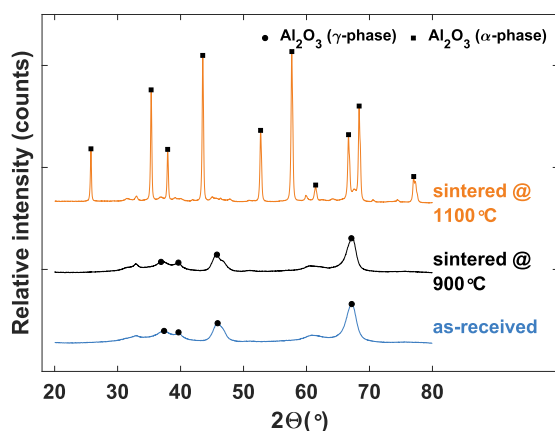|	SA (m^2 g^{-1})	
	Al_2O_3	CeO_2
As-received	150.40	33.40
Sintered at 900 °C	124.00	1.85
Sintered at 1100 °C	29.90	0.70

Fig. 5. Evolution of the crystal phases in the γ-Al_2O_3 powder with increasing sintering temperatures. XRD analyses of the as-received (blue curve), and sintered at 900 °C (black curve) and 1100 °C (orange curve) alumina powders. Transformation from γ- to α-Al_2O_3 was confirmed during sintering at 1100 °C.

presented in Fig. 5, providing information on the crystalline phases.

The X-ray diffractogram of the as-received alumina powder (blue curve) revealed main characteristic peaks at 2θ = 37 °, 39 °, 45 °, and 67 °. The identified peaks matched with the γ-Al_2O_3 standard obtained from the database, confirming that the as-received powder consisted solely of γ-phase. The overlapping curves associated with the as-received (blue curve) and sintered at 900 °C (black curve) alumina powders suggested stable retention of the γ-phase in the case of sintering at 900 °C. Moreover, the width of the main peaks is similar in both the blue curve and the black curve, indicating that no significant crystallite size growth occurred at the sintering temperature of 900 °C.

On the other hand, the X-ray diffractogram of sintered powder at 1100 °C (orange curve) with remarkably strong and sharp peaks was correspondent to the α-phase, whereas the peaks attributed to the γ-phase were hardly observable. The obtained results in the case of sintering at 1100 °C indicated phase transformation from γ- to α-Al_2O_3. Hence, the huge reduction in the SA and significant particle size growth of the as-received γ-Al_2O_3 powder at 1100 °C are now confirmed to be related to the presence of the α-phase. Besides the main sharp peaks associated with the α-phase, many small bumps, which are due to the presence of other transition phases such as the θ-phase, can be observed in the orange curve. This also justifies the obtained SA result (29.90 m^2 g^{-1}) for the sintered alumina powder at 1100 °C, which is relatively larger than the typical SA for pure α-Al_2O_3 (2–10 m^2 g^{-1}).

Similarly, the evolution of the crystal phases in the CeO_2 powder with increasing sintering temperatures was studied. The obtained XRD analyses of the as-received (blue curve) as well as sintered at 900 °C (black curve) and 1100 °C (orange curve) ceria powders are presented in Fig. 6. The achieved results revealed no
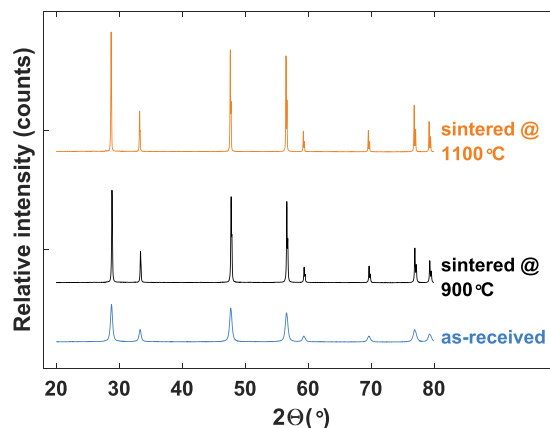

Fig. 6. Evolution of the crystal phases in the CeO_2 powder with increasing sintering temperatures. XRD analyses of the as-received (blue curve), and sintered at 900 °C (black curve) and 1100 °C (orange curve) ceria powders. No phase transformation was observed for the studied sintering temperatures.

phase transformation for the studied sintering temperatures because the peaks between different heat treatments matched. One can also notice that the main peaks for the CeO_2 powder became narrower and sharper by increasing the sintering temperature, indicating that crystallite size growth already happened at 900 °C and continued even at 1100 °C.

Based on the achieved results from TEM, BET, and XRD characterizations, it was concluded that γ-Al_2O_3 has a phase change between 900 °C and 1100 °C. It was further investigated whether the CeO_2 contained in the printed structures prohibits the phase transition of γ-Al_2O_3 (discussed in Section 3.6).

3.1.4. Dilatometric analysis

To optimize the heat treatment of the printed structures, containing γ-Al_2O_3 and CeO_2, it is necessary to have knowledge about the thermal behavior of each powder as well as their relative length change during sintering. This is why the dilatometric analysis of the as-received powders was performed. As shown in Fig. 7, under the same heat treatment procedure for both powders, a higher initiation temperature for sintering was observed for γ-Al_2O_3 ($\sim$ 900 °C) in comparison to CeO_2 ($\sim$ 700 °C). However, it was found that both powders had an almost similar reduction in relative length ($\sim$ 14%) after sintering at 1100 °C.

3.2. Rheological behavior of the prepared ceramic resins

In CSL, having a low viscosity is one of the main requirements of a ceramic resin to be printable. Commonly, a viscosity of 3 Pa·s at a shear rate of 10 s^{-1} is recommended as an upper limit for this purpose. Furthermore, ceramic resins should exhibit shear-thinning behavior, which is essential for printing [23]. The rheological behavior of the raw resin and the prepared ceramic resins (formulation of the ceramic resins can be found in Table 1) was studied to investigate their printability. The viscosity of the resins versus shear rate is shown in Fig. 8. As can be seen, the addition of the ceramic powders to the raw resin significantly increased the viscosity. Moreover, this figure shows that the prepared ceramic resins revealed a shear-thinning behavior within the shear rate region of 1–1000 s^{-1}. The R_1 resin, consisting of 20 vol% of γ-Al_2O_3, had a viscosity of 3.47 Pa.s at a shear rate of 10 s^{-1}. Further addition of γ-Al_2O_3 powder to the resin decreased the fluidity of the ceramic resin which might be due to the high surface area of the powder and the hydroxyl groups on its surface. That is why 20 vol% was chosen as the maximum solid content for the R_1 resin.
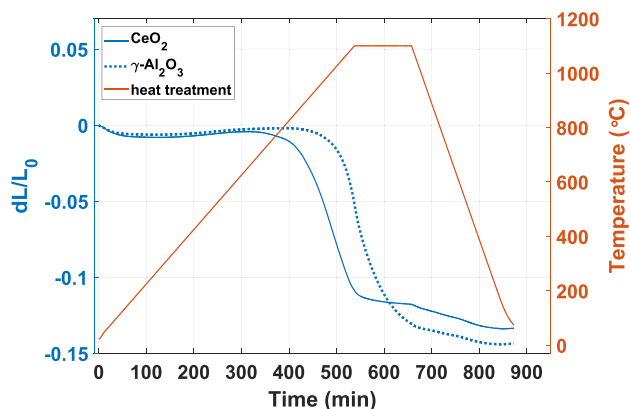
Fig. 7. Dilatometry measurements of pressed γ-Al$_2$O$_3$ (dashed blue line) and CeO$_2$ (solid blue line) powders, and the heat treatment program (solid orange line) used in the measurements. Relative length change (dL/L$_0$ in % (left y-axis)) versus time as well as temperature (right y-axis) versus time.
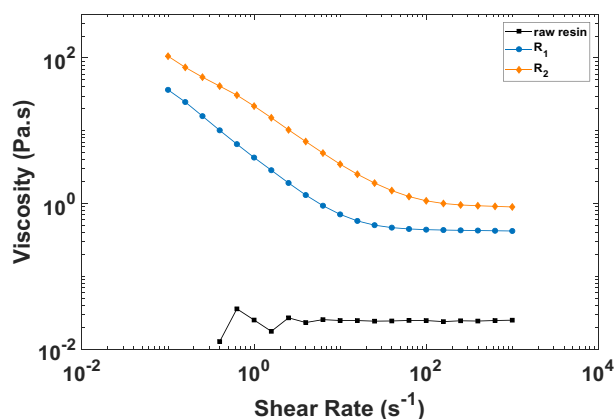

Fig. 8. Viscosity as a function of shear rate for the pure resin, R$_1$, and R$_2$ resins.

In traditional catalytic converters, typically the washcoat layer is composed of 60–85 wt% of γ-Al$_2$O$_3$ and 40–15 wt% of other ceramics, such as ceria, zirconia, and lanthana. To demonstrate whether it is possible to fabricate self-standing structures out of washcoat materials, alumina (60 wt%) and ceria (40 wt%) were selected as the two components of the washcoat composition. Accordingly, the R$_2$ resin, consisting of 15 vol% of γ-Al$_2$O$_3$ and 5 vol% of CeO$_2$, was prepared. It was found out that this ceramic resin had a viscosity of 0.71 Pa.s at a shear rate of 10 s^{-1}, indicating its printablity.

3.3. Photocuring behavior of the prepared ceramic resins and the printing process

In CSL, the utilization of ceramic powders with low or medium RI is more recommended. Moreover, the ceramic powder should not have high light adsorption since light must penetrate through the ceramic resin for the photopolymerization process [23]. In this study, it was aimed to employ CeO$_2$, which has a high RI, and γ-Al$_2$O$_3$, which has a low RI, in CSL. To assess the effect of CeO$_2$ in the photopolymerization process, two different resins were prepared: a plain γ-Al$_2$O$_3$ resin (R$_1$) and a CeO$_2$-doped γ-Al$_2$O$_3$ resin (R$_2$).

3.3.1. Resin R$_1$

Although extensive research has been carried out on the fabrication of dense alumina (α-Al$_2$O$_3$) parts via CSL, only one research

[25] has reported the fabrication of mullite structures via digital light processing of a preceramic polysiloxane with active γ-Al$_2$O$_3$ fillers. Therefore, further research has to be conducted on the preparation of printable γ-Al$_2$O$_3$ resins due to the different physical and surface chemical properties of γ-Al$_2$O$_3$ versus α-Al$_2$O$_3$.

The working curve associated to the R$_1$ resin, which contained 20 vol% of γ-Al$_2$O$_3$, is shown as the black curve in Fig. 9. Calculating the slope and intercept of the curve, D$_p$ and E$_c$ were found to be 408.06 μm and 37.55 mJ cm^{-2}, respectively. This relatively large D$_p$ can be justified by the fact that this ceramic resin had a low volume fraction (20 vol%) of the porous γ-Al$_2$O$_3$ powder. The low volume fraction of the porous powder allows light to penetrate deep into the resin and cure a thick layer.

The edges of the printed parts made from the R$_1$ resin were not sharp, which is due to the deep penetration of the light through this resin, leading to inaccurate printing. Although C$_d$ can be adjusted by controlling the exposure time, it is not always sufficient to reduce the exposure time to achieve a low C$_d$ as the penetration of light through the resin is even possible within a short time. Therefore, it is highly recommended to vary the resin formulation for a reduction in D$_p$. Schmidt et al. [25] used an azo dye as a photo-absorber to control the penetration depth of the light through the resin with active γ-Al$_2$O$_3$ fillers. In this study, it was investigated how ceria, which is commonly used in the catalyst support materials of CCs, affects the photocuring behavior of the R$_1$ resin.

3.3.2. Resin R$_2$

To vary the formulation of the R$_1$ resin, a new ceramic resin (R$_2$) was prepared by substituting 5 vol% of the alumina powder with ceria, keeping the total volume fraction of the powder constant (20 vol%). From C$_d$ measurements, shown as the red curve in Fig. 9, D$_p$ and E$_c$ were found to be 75.20 μm and 20.75 mJ cm^{-2}, respectively. It was observed that the addition of ceria significantly decreased D$_p$ of the R$_1$ resin from 408.06 μm to 75.20 μm. To understand better what causes the remarkable reduction in D$_p$ upon the addition of ceria to the alumina resin, one has to consider the parameters that affects D$_p$. In the presence of particles that scatter the light in the resin medium, D$_p$ is proportional to certain parameters as follows [26]:

$$D_p \propto \frac{d}{\phi \, \Delta n^2} \tag{5}$$

where d is the average particle size of the powder; ϕ is the volume fraction of the powder; and Δn is the refractive index (RI) contrast,
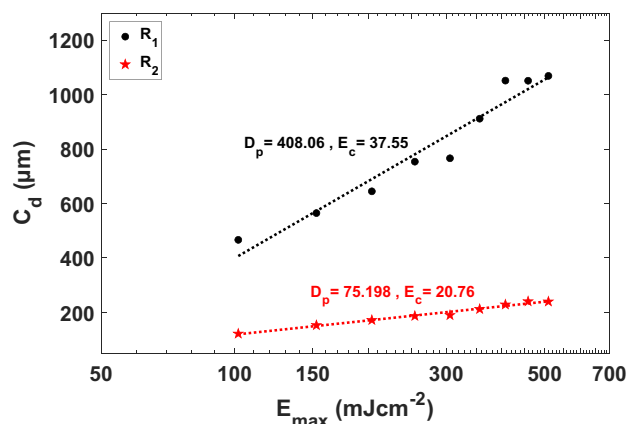

Fig. 9. Curing depth (C$_d$) versus energy dose (E$_{max}$) for the R$_1$ and R$_2$ resins.

which is the difference between the RIs of the suspended ceramic particles (n_0) and the liquid resin (n_0).

As indicated by Eq. 5, D_p is inversely proportional to the square of Δn and proportional to the particle size. Ceria has smaller particle size in comparison to alumina, and therefore, it reduces D_p. Moreover, ceria has a high RI of 2.35 [27,28]. The addition of ceria to alumina, which has a lower RI (1.7), increases the RI contrast (Δn), resulting in a lower D_p. As schematically illustrated in Fig. 10, ceria particles with a higher RI, scatter light at larger angles of deflection in comparison to alumina particles, which scatter light in smaller angles. This phenomenon suppresses the light penetration through the ceramic resin and consequently, reduces D_p. Therefore, ceria significantly disrupts photopolymerization when added to the (R_1) resin due to its stronger light scattering and smaller particle size.

3.4. TG analysis

Major surface flaws and delamination may occur during the debinding of the as-printed structures. Fast heating rates can delaminate the printed structure and create bubbles on its surface. Therefore, debinding must be done with slow heating rates and appropriate dwelling time at critical temperatures; otherwise, it leads to poor quality for the final structure. The critical temperatures are those at which fast degradation of the cured resin happens and can be identified from TG studies.

Fig. 11 shows the thermal degradation behavior of the as-printed structure made from the R_2 resin during TG analysis. This figure depicts a decreasing relative sample mass as the blue thermogravimetry (TG) curve and its corresponding mass rate loss (first derivative of TG) as the orange derivative thermogravimetry (DTG) curve, both as functions of temperature. TG analysis showed that mass loss started already below 234 °C, and it is primarily due to the diffusion and evaporation of the additives, unreactive diluents, and uncured monomers. Moreover, one can notice a slow degradation happening from 234 °C to 315 °C, which is due to the presence of the selected acrylates as the major component used in the resin. More noticeably, the DTG curve shows a clear maximum in the mass loss rate around 400 °C, representing the fast degradation of polyacrylates used in the raw resin at this temperature [29].
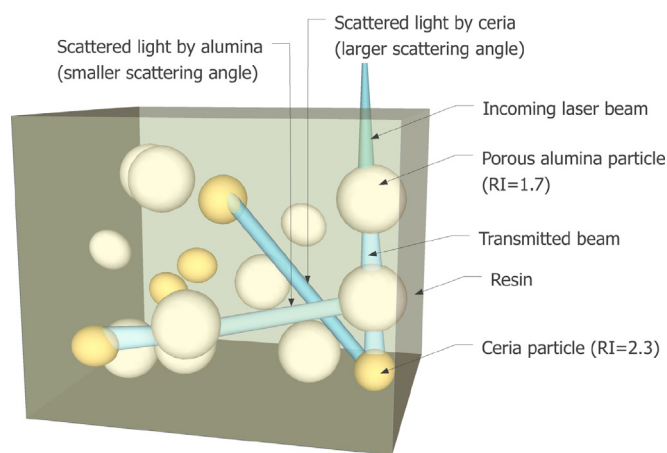

Fig. 10. Simple schematic view of the scattered light (only in one direction) by the porous alumina particle (white particle) and by the ceria particle (yellow particle) in the resin medium. Alumina particles, having a lower RI and larger particle size, scatter light at lower angles in comparison to ceria particles, which have a higher RI and smaller particle size. Large deflection angles of ceria suppress the light penetration and reduce the D_p of the resin.
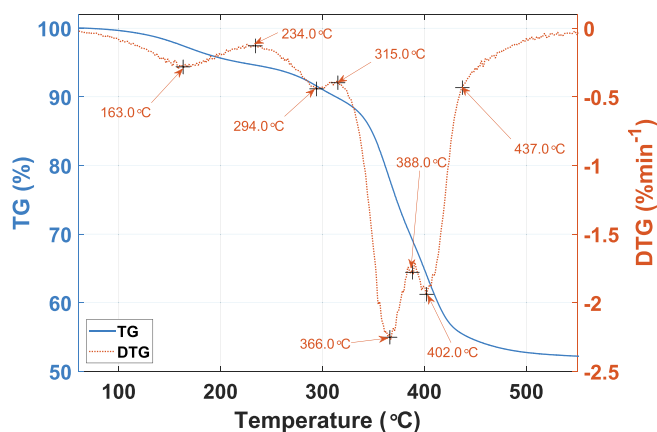

Fig. 11. TG analysis showing relative sample mass (TG) and mass loss rates (DTG) of the as-printed structure made from the R_2 resin.

Based on the obtained results from TG analysis, an appropriate heat treatment program was selected for debinding of the as-printed structure, which included very slow heating rates and proper dwelling times between 234 °C and 400 °C.

3.5. Characterizations of the printed structures

To evaluate the use of CSL for the fabrication of hierarchical porous structures for catalytic conversion applications, two honeycomb and twisted-honeycomb structures, whose fabrication via conventional methods is nearly impossible, were printed and sintered. The as-printed structures are shown in Fig. 12(a). The printed structures were then characterized by the following techniques.

3.5.1. Analytical electron microscopy

One of the aims in this study was to investigate if alumina and ceria were dispersed homogeneously in the structure, and that is why SEM-EDS mapping was used to visualize the microscale spatial distribution of alumina and ceria particles within the imaged area of the as-printed structures. As can be seen from the superimposition image in Fig. 12(b), the orange-colored alumina particles could clearly be distinguished from the cyan-colored ceria particles. The obtained results also revealed the presence of O and C elements. As mentioned earlier, SEM imaging was carried out in low vacuum conditions without any conductive coating, and therefore, it can be stated that C is not from carbon coating but the cured resin. Additionally, a backscattered electron (BSE) SEM image was used to assess the elemental distribution within the cross-sectional region across consecutive layers. Fig. 12(c) shows the BSE atomic number or Z-contrast image of the studied area. This image shows that Ce, which has a higher atomic number compared to Al and therefore appears as brighter particles, was evenly distributed within the layers. This confirms that ceria did not sediment in the resin during the printing process. This image also demonstrates that each printed layer had been accurately attached to the previously-cured layer.

After sintering at both 900 °C and 1100 °C, the final printed honeycomb structures remained intact and only underwent shrinkage. Fig. 13(a) shows the printed structure sintered at 1100 °C versus the as-printed structure. After two-step heat treatment process (debinding and sintering), the structure sintered at 1100 °C underwent more shrinkage (14.3 %) in both X and Y directions than the structure sintered at 900 °C (3.1 %). Furthermore, it was aimed to study how sintering affected the distribution of the two powders. Therefore, SEM-EDS was used to assess the elemental distribution
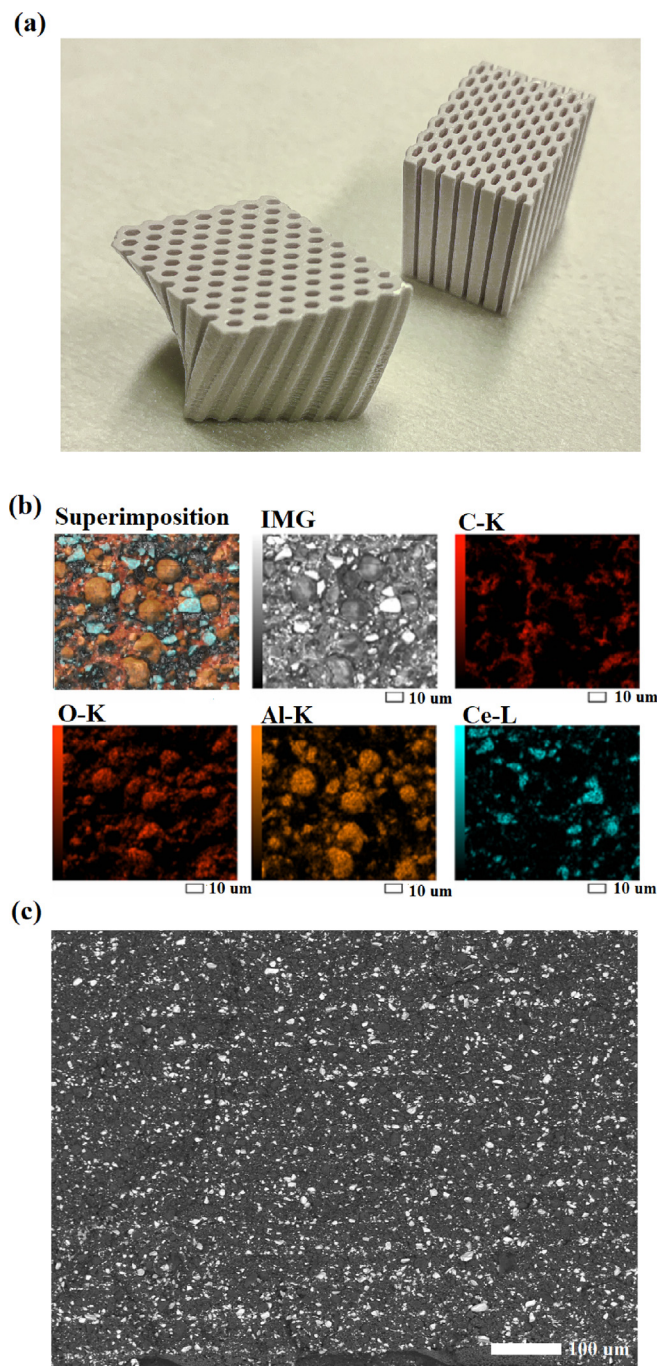
(a)

(b)

(c)

Fig. 12. (a) Photograph of the honeycomb and twisted honeycomb as-printed structures made from the R₂ resin with a layer thickness of 50 μm and a curing depth of 250 μm; (b) Microscale elemental distribution of the as-printed structure by SEM-EDS with six sub-images: superimposition of all elemental maps, BSE image of the studied area, and individual elemental maps of C (red), O (rust), Al (orange), and Ce (cyan) shown in the remaining sub-images; (c) BSE image of the cross-sectional region of the as-printed structure. Images (b) and (c) were taken using BED-C detector and low vacuum mode (10 Pa).

and cross-sectional morphology of the sintered structures. The microscale elemental distribution of the same structure obtained by SEM-EDS is presented in Fig. 13(b). The results indicated a homogeneous distribution of alumina (orange particles) and ceria (cyan particles) within the structure. Moreover, the distinction of each printed layer can be observed, which might have occurred after debinding, due to the low powder content within the as-printed structure (20 vol%).

In this research, it was also investigated whether the sintered structures possess hierarchical porosity, which is essential for catalytic reactions. A hierarchical porous structure must contain pores on two or more length scales [30]. The hierarchical porosity of the structure sintered at 1100 °C was characterized by SEM, as sown in Fig. 14. As can be seen from Fig. 14(a), the structure comprised of pores ($\approx$ 1 mm, level-I pore) in the form of open channels which enable gas flow through the structure. A higher magnification from the surface of the channel (Fig. 14(b)) suggests the presence of interconnected pores (< 10 μm, level-II pore) between the agglomerates. Moreover, the structure contains pores between the primary particles; the pore size is below or close to the primary particle size (10–100 nm, level-III pore). Therefore, it can be stated that the printed structure possessed hierarchical porosity.

3.5.2. BET and XRD analyses

Having a high surface area is an important requirement for catalytic converters. Therefore, the SA of each sintered structure was studied using BET analysis. The measurements showed that the printed structure sintered at 900 °C possessed a higher SA (82.00 m² g⁻¹) in comparison to the case of sintered at 1100 °C (46.80 m² g⁻¹).

Additionally, the effect of sintering temperature on the phase transition occurring during sintering of the printed structures was studied. Fig. 15 shows the XRD patterns obtained for the printed structures sintered at 900 °C (blue curve) and 1100 °C (orange curve). Phase identification analysis revealed that only ceria and the γ-phase of alumina were present in the diffractogram of the sintered structure at 900 °C. On the other hand, the diffractogram of the sintered structure at 1100 °C revealed the sharp and distinct peaks associated to the α-phase of alumina as well as the peaks for ceria, whereas the peaks for γ-phase were less visible. Moreover, few tiny peaks, which are corresponding to the θ-phase of alumina, can be seen in the same diffractogram, justifying the achieved SA result (46.80 m² g⁻¹) for the structure sintered at 1100 °C.

3.6. Stabilizing effect of CeO_2 *on* γ-Al_2O_3

The extent of stabilization of ceria on γ-Al_2O_3 depends on several factors, such as temperature, atmosphere, and the added amount of ceria (loading). It has been reported that the stabilizing effect of ceria under oxidizing conditions is noticable only in a narrow temperature range around 1100 °C, and it relies on loadings. The reported ranges for temperature and loadings vary from study to study [12]. Although this effect has been extensively studied in conventional methods, such as mixing sol-gel derived alumina and ceria gel precursors [31], no study has thus far reported the same effect in the case of 3D printing of the two powders. Thus, the stabilizing effect of ceria on γ-Al_2O_3 at each sintering temperature was investigated by comparing the SA of the printed structure to that of the pure Al_2O_3 (refer to Table 2). Moreover, analytical electron microscopy was used to investigate this effect more in-depth.

Table 3 summarizes the BET SA measurements of the pure γ-Al_2O_3 powder, the pure CeO_2 powder, and the printed structure (made of 60 wt% alumina and 40 wt% ceria) after sintering under air for 2 h at 900 °C and 1100 °C. From the achieved results in this work for SA, it was observed that the SA of the printed structure (82.00 m² g⁻¹) was less than the SA of the pure Al_2O_3 (124.00 m² g⁻¹) in case of sintering at 900 °C. Therefore, it can be concluded that ceria did not stabilize the surface area of alumina at 900 °C. This drop in SA upon the addition of ceria to alumina can be related to the high density and low porosity of ceria. The SA of the printed structure is referred to 1 g of the printed structure, consisting of 0.6 g of alumina and 0.4 g of ceria. Assuming that
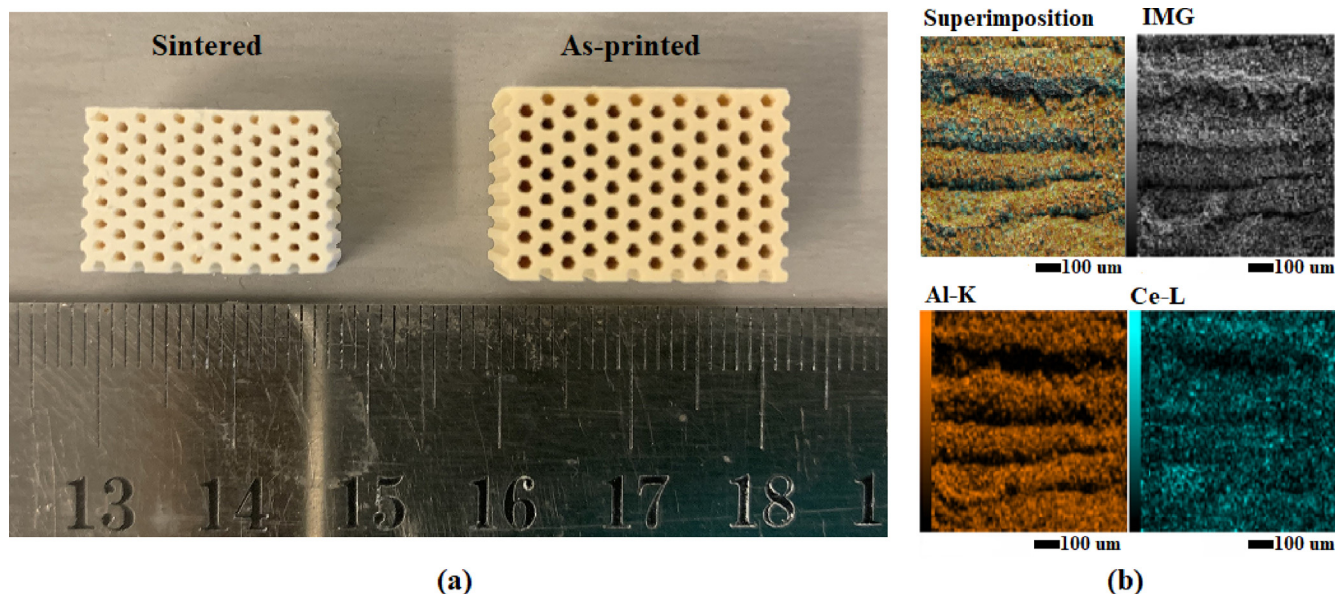
Fig. 13. (a) Photograph of the final honeycomb structure sintered at 1100 ° next to the as-printed structure shows a shrinkage of 14.3% in X and Y directions; (b) Microscale elemental distribution of the sintered structure obtained by SEM-EDS in low vacuum mode (10 Pa) with four subimages: superimposition of all elemental maps, secondary electron (SE) image of the studied area, and individual elemental maps of Al (orange) and Ce (cyan) shown in the remaining subimages.
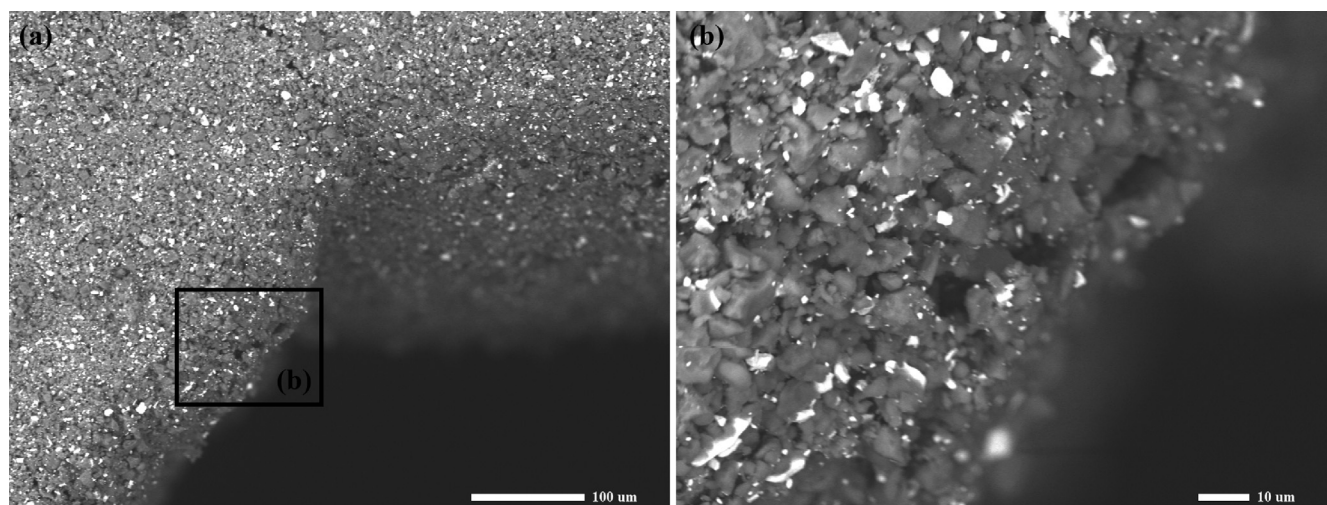

Fig. 14. (a) BSE image of the printed structure sintered at 1100 °C obtained by SEM in low vacuum mode (10 Pa) with a magnification of 220X; (b) Higher magnification (1000X) BSE image of the marked region in image (a) suggests the presence of interconnected pores in the porous structure.

the SA of ceria is unaffected by alumina, the SA of alumina contained in the printed structure was calculated to be 135.5 $m^2\ g^{-1}$ after sintering at 900 °C. This is comparable to the SA of the pure Al_2O_3 (124.00 $m^2\ g^{-1}$) sintering at the same temperature.

The (S) TEM images, shown in Figs. 16(a)-(c), were in accordance with SA results. Fig. 16(a) shows a STEM bright field image of the printed structure sintered at 900 °°C, and Fig. 16(b) shows the elemental distribution of the same imaged area obtained by STEM-EDS. The green-colored faceted ceria particles are distinguished from red-colored alumina particles in this superimposition image. Fig. 16(c) shows a high resolutional TEM image of pure alumina powder sintered at 900 °C. Comparing Figs. 16(a)-(b) with Fig. 16(c), no significant variation in the particle size of alumina can be observed upon the addition of ceria, indicating that ceria was not very effective in stabilization of γ-Al_2O_3 at 900 °C.

On the other hand, the SA of the printed structure (46.80 $m^2\ g^{-1}$) was higher than the SA of the pure Al_2O_3 (29.90 $m^2\ g^{-1}$) in case of sintering at 1100 °C, confirming that ceria has partially stabilized γ-Al_2O_3. The SA of alumina contained in the printed structure was calculated to be 77.5 $m^2\ g^{-1}$, which is incomparable to the SA of the pure Al_2O_3 (29.90 $m^2\ g^{-1}$) at 1100 °C.

This result was also in good agreement with the (S) TEM results. Fig. 16(d) shows an STEM bright field image of the printed structure sintered at 1100 °C, and Fig. 16(e) shows the elemental distribution of alumina (red particles) and ceria (green particles) within the same imaged area. Fig. 16(f) shows a TEM image of pure alumina powder sintered at 1100 °C. From Figs. 16(d)-(e), it can be stated that the presence of faceted ceria particles in the final printed structure hindered the particle size growth of alumina at 1100 °C. As proposed by Humbert et al. [32] and clearly shown
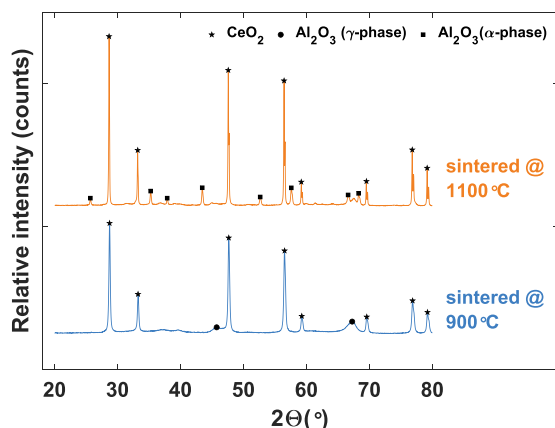
Fig. 15. Evolution of the crystal phases in the printed structure with increasing sintering temperatures. XRD analyses of the printed structure with sintering temperature of 900 °C (blue curve) and 1100 °C (orange curve).

Table 3
SA obtained by BET analyses associated with the pure Al_2O_3 and CeO_2 powders, and the printed structure. Samples were sintered at 900 °C and 1100 °C.

	SA ($m^2\ g^{-1}$)		
T (°C)	Pure Al_2O_3	Pure CeO_2	Printed structure
900	124.00	1.85	82.00 (135.5)[a]
1100	29.9	0.70	46.80 (77.5)

[a] Values in parentheses indicate the SA of Al_2O_3 contained in the printed structure.

in Fig. 16(e), the reason for stabilization can be correlated to the geometrical arrangement of the particles containing cerium, which form microdomains on the boundaries of alumina particles and may act as barriers for surface diffusion. In contrast, a remarkable

increase in the particle size of alumina was observed in the absence of ceria particles at 1100 °C (see Fig. 16(f)).

This is a remarkable result, showing that the stabilizing effect of ceria on alumina works in 3D-printing of the two powders in the same way as in conventional methods. This is very promising for catalytic research as it gives the possibility to fabricate complex structures with high SA and good physical stability by optimizing the sintering temperature and the added amount of ceria.

4. Conclusion

In summary, CSL was used to fabricate hierarchical porous ceramic structures made of γ-Al_2O_3-CeO_2, which are aimed to be further used in catalytic applications. The printed structures were sintered at two different temperatures (900 °C and 1100 °C). The microstructure characterizations of the final printed structures obtained by SEM-EDS and (S) TEM-EDS confirmed that both powders were homogeneously distributed within the structure.

To fabricate such structures, a novel photocurable ceramic resin (R_2) was prepared by dispersing γ-Al_2O_3 (15 vol%) and CeO_2 (5 vol %) into an environment-friendly raw resin (a mixture of acrylate-based monomers). In addition to this resin, another photocurable plain γ-Al_2O_3 (20 vol%) resin (R_1) was prepared to assess the effect of ceria on the photopolymerization process. C_d measurements revealed that upon the addition of 5 vol% of ceria, which has a high refractive index and smaller particle size, D_p of the R_1 resin significantly decreased from 408.06 μm to 75.20 μm. This was advantageous in the case of the R_1 resin, which had a large D_p resulting in poor printing accuracy. Furthermore, it was shown that ceria not only reduced the large D_p of γ-Al_2O_3 but also stabilized the surface area of the printed γ-Al_2O_3 at high temperatures. The investigations of the stabilizing effect of ceria on printed γ-Al_2O_3 revealed that ceria partially stabilized the printed γ-Al_2O_3 at 1100 °C, whereas the same effect was not observed at 900 °C. This was a promising result, indicating that the stabilizing effect of ceria, or
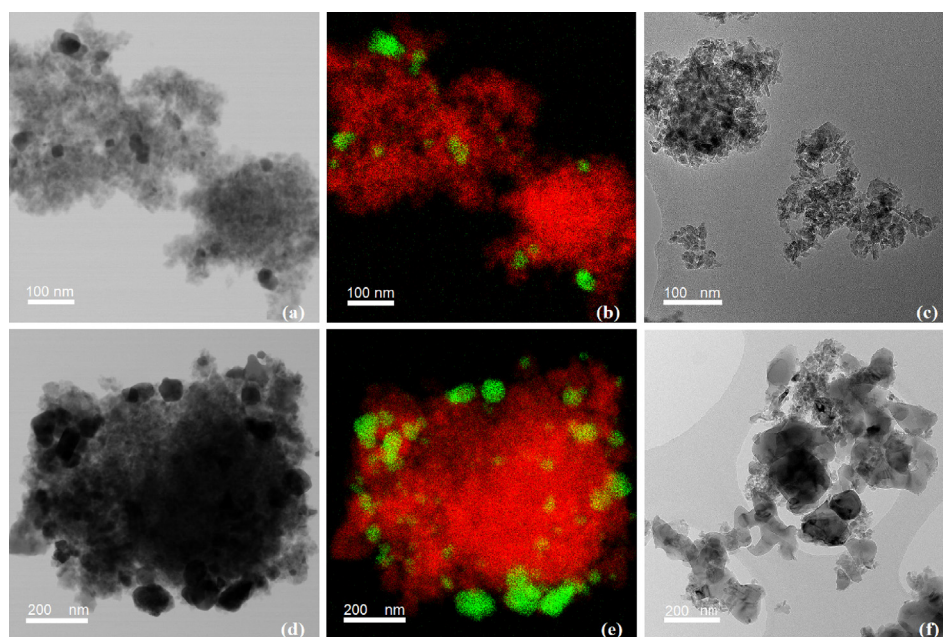

Fig. 16. (a) STEM bright field image of the printed structure sintered at 900 °C; (b) Elemental distribution obtained by STEM-EDS for the same imaged area as in image (a) with red particles indicating alumina and green particles indicating ceria; (c) TEM image of the pure alumina powder sintered at 900 °C; (d) STEM bright field image of the printed structure sintered at 1100 °C; (e) Elemental distribution obtained by STEM-EDS for the same imaged area as in image (d) with red particles indicating alumina and green particles indicating ceria; (f) TEM image of the pure alumina powder sintered at 1100 °C. Different magnifications have been used for the first (a-c) and second (d-f) row of images.

perhaps any other stabilizer, on γ-Al_2O_3 works in 3D-printing of the powders as well.

This study also reflected on the balance between having a high SA and achieving good physical stability in the printed structures, which are essential requirements for any catalytic applications. Strong structures require sintering at high temperatures; however, this leads to a decrease in surface area in the case of γ-Al_2O_3. Although the printed structure sintered at 1100 °C was physically stronger than the structure sintered at 900 °C, it possessed a lower SA (46.80 m^2 g^{-1} vs. 82.00 m^2 g^{-1}), which is undesirable for our future application. However, further research into the stabilizer could find an optimized combination that stabilizes the printed alumina when sintered above 900 °C and achieves a strong structure that also has a high SA. Then it could be possibe to fabricate strong and curved self-supporting structures, which would increase the residence time and mass transfer of the pollutants within the structure.

The printed structures in this study are intended to be further coated by precious metals to assess their catalytic efficiency. Furthermore, the success in using CSL to print multiple oxide ceramics for the manufacture of components with complex designed geometries suggests that greater performance enhancements for catalytic applications are possible, thus motivating further investigations as the next steps of this study.

Declaration of Competing Interest

The authors declare that they have no known competing financial interests or personal relationships that could have appeared to influence the work reported in this paper.

Acknowledgements

References

[1] S. Li, J. Deng, Y. Dan, L. Xiong, J. Wang, Y. Chen, Designed synthesis of highly active CeO_2 - ZrO_2 - Al_2O_3 support materials with optimized surface property for pd-only three-way catalysts, Appl. Surf. Sci. 506 (2020) 144866, https://doi.org/10.1016/j.apsusc.2019.144866.

[2] M. Laurenzi, R. Spigler, Geometric effects in the design of catalytic converters in car exhaust pipes, Math. Ind. Case Stud. 9 (1) (2018) 1, https://doi.org/10.1186/s40929-018-0018-2.

[3] N. Jeyakumar, C. Arumugam, B. Narayanasamy, R. Rajkumar, Effect of wash coat layers on the conversion efficiency of a catalytic converter in the si engine, Int. J. Ambient Energy (2020) 1–9, https://doi.org/10.1080/01430750.2020.1712256.

[4] P. Jiang, G. Lu, Y. Guo, Y. Guo, S. Zhang, X. Wang, Preparation and properties of a γ-al2o3 washcoat deposited on a ceramic honeycomb, Surf. Coat. Technol. 190 (2–3) (2005) 314–320, https://doi.org/10.1016/j.surfcoat.2004.05.029.

[5] H. Santos, M. Costa, Analysis of the mass transfer controlled regime in automotive catalytic converters, Int. J. Heat Mass Transf. 51 (1–2) (2008) 41–51, https://doi.org/10.1016/j.ijheatmasstransfer.2007.04.044.

[6] C. Agrafiotis, A. Tsetsekou, The effect of powder characteristics on washcoat quality. part i: Alumina washcoats, J. Eur. Ceram. Soc. 20 (7) (2000) 815–824, https://doi.org/10.1016/S0955-2219(99)00218-6.

[7] I. Amato, D. Martorana, B. Silengo, Sintering of pelleted catalysts for automotive emission control, in: Sintering and Catalysis, Springer, 1975, pp. 187–197.

[8] M. Bodaghi, A. Mirhabibi, H. Zolfonun, M. Tahriri, M. Karimi, Investigation of phase transition of γ-alumina to α-alumina via mechanical milling method,

[9] Phase Trans. 81 (6) (2008) 571–580, https://doi.org/10.1080/01411590802008012.

[9] S. Lamouri, M. Hamidouche, N. Bouaouadja, H. Belhouchet, V. Garnier, G. Fantozzi, J.F. Trelkat, Control of the γ-alumina to α-alumina phase transformation for an optimized alumina densification, Boletín de la sociedad española de cerámica y vidrio 56 (2) (2017) 47–54, https://doi.org/10.1016/j.bsecv.2016.10.001.

[10] A.S. Kumar, A.R. Durai, T. Sornakumar, Development of alumina–ceria ceramic composite cutting tool, Int. J. Refract. Met. Hard Mater. 22 (1) (2004) 17–20, https://doi.org/10.1016/j.ijrmhm.2003.10.005.

[11] S. Adamu, M.Y. Khan, S.A. Razzak, M.M. Hossain, Ceria-stabilized meso- Al_2O_3: synthesis, characterization and desorption kinetics, J. Porous Mater. 24 (5) (2017) 1343–1352, https://doi.org/10.1007/s10934-017-0376-3.

[12] A. Piras, A. Trovarelli, G. Dolcetti, Remarkable stabilization of transition alumina operated by ceria under reducing and redox conditions, Appl. Catal. B: Environ. 28 (2) (2000) L77–L81, https://doi.org/10.1016/S0926-3373(00)00226-5.

[13] T. Shamim, The effect of space velocity on the dynamic characteristics of an automotive catalytic converter, SAE Trans. (2005) 974–982. https://www.jstor.org/stable/44721016.

[14] A. Martin, N. Will, A. Bordet, P. Cornet, C. Gondoin, X. Mouton, Effect of flow distribution on emissions performance of catalytic converters, SAE Trans. (1998) 384–390. https://www.jstor.org/stable/44746459.

[15] O. Laguna, P. Lietor, F.I. Godino, F. Corpas-Iglesias, A review on additive manufacturing and materials for catalytic applications: milestones, key concepts, advances and perspectives, Mater. Des. (2021) 109927, https://doi.org/10.1016/j.matdes.2021.109927.

[16] C.R. Tubío, J. Azuaje, L. Escalante, A. Coelho, F. Guitián, E. Sotelo, A. Gil, 3D printing of a heterogeneous copper-based catalyst, J. Catal. 334 (2016) 110–115, https://doi.org/10.1016/j.jcat.2015.11.019.

[17] D. Liu, P. Jiang, X. Li, J. Liu, L. Zhou, X. Wang, F. Zhou, 3d printing of metal-organic frameworks decorated hierarchical porous ceramics for high-efficiency catalytic degradation, Chem. Eng. J. 397 (2020) 125392, https://doi.org/10.1016/j.cej.2020.125392.

[18] Y. Jiang, F.-Q. Jiang, X. Liao, S.-L. Lai, S.-B. Wang, X.-Q. Xiong, J. Zheng, Y.-G. Liu, Customized three-dimensional porous catalyst for knoevenagel reaction, J. Porous Mater. 27 (3) (2020) 779–788, https://doi.org/10.1007/s10934-020-00859-3.

[19] X. Zhou, C.-J. Liu, Three-dimensional printing of porous carbon structures with tailorable pore sizes, Catal. Today 347 (2020) 2–9, https://doi.org/10.1016/j.cattod.2018.05.044.

[20] A. Potdar, L.C. Thomassen, S. Kuhn, Scalability of 3d printed structured porous milli-scale reactors, Chem. Eng. J. 363 (2019) 337–348, https://doi.org/10.1016/j.cej.2019.01.082.

[21] M.J. Regufe, A.F. Ferreira, J.M. Loureiro, A. Rodrigues, A.M. Ribeiro, Electrical conductive 3d-printed monolith adsorbent for co2 capture, Micropor. Mesopor. Mater. 278 (2019) 403–413, https://doi.org/10.1016/j.micromeso.2019.01.009.

[22] N. Merilaita, T. Vastamäki, A. Ismailov, E. Levänen, M. Järveläinen, Stereolithography as a manufacturing method for a hierarchically porous zsm-5 zeolite structure with adsorption capabilities, Ceram. Int. 47 (8) (2021) 10742–10748, https://doi.org/10.1016/j.ceramint.2020.12.190.

[23] S. Zakeri, M. Vippola, E. Levänen, A comprehensive review of the photopolymerization of ceramic resins used in stereolithography, Addit. Manuf. (2020) 101177, https://doi.org/10.1016/j.addma.2020.101177.

[24] Y. Liu, Z. Chen, J. Li, B. Gong, L. Wang, C. Lao, P. Wang, C. Liu, Y. Feng, X. Wang, 3d printing of ceramic cellular structures for potential nuclear fusion application, Addit. Manuf. (2020) 101348, https://doi.org/10.1016/j.addma.2020.101348.

[25] J. Schmidt, A.A. Altun, M. Schwentenwein, P. Colombo, Complex mullite structures fabricated via digital light processing of a preceramic polysiloxane with active alumina fillers, J. Eur. Ceram. Soc. 39 (4) (2019) 1336–1343, https://doi.org/10.1016/j.jeurceramsoc.2018.11.038.

[26] M.L. Griffith, J.W. Halloran, Freeform fabrication of ceramics via stereolithography, J. Am. Ceram. Soc. 79 (10) (1996) 2601–2608, https://doi.org/10.1111/j.1151-2916.1996.tb09022.x.

[27] F. Goubin, X. Rocquefelte, M.-H. Whangbo, Y. Montardi, R. Brec, S. Jobic, Experimental and theoretical characterization of the optical properties of CeO_2, $SrCeO_3$, and Sr_2CeO_4 containing Ce^{4+} (f^0) ions, Chem. Mater. 16 (4) (2004) 662–669, https://doi.org/10.1021/cm034618u.

[28] M. Mogensen, N.M. Sammes, G.A. Tompsett, Physical, chemical and electrochemical properties of pure and doped ceria, Solid State Ionics 129 (1–4) (2000) 63–94, https://doi.org/10.1016/S0167-2738(99)00318-5.

[29] T. Vastamäki, Stereolithography 3D-printing of ceramics (Master's thesis), Tampere University, 2019.

[30] P. Colombo, C. Vakifahmetoglu, S. Costacurta, Fabrication of ceramic components with hierarchical porosity, J. Mater. Sci. 45 (20) (2010) 5425–5455, https://doi.org/10.1007/s10853-010-4708-9.

[31] K.M. Khalil, Synthesis and characterization of mesoporous ceria/alumina nanocomposite materials via mixing of the corresponding ceria and alumina gel precursors, J. Colloid Interface Sci. 307 (1) (2007) 172–180, https://doi.org/10.1016/j.jcis.2006.11.039.

[32] S. Humbert, A. Colin, L. Monceaux, F. Oudet, P. Courtine, Simultaneous atmosphere and temperature cycling of three-way automotive exhaust catalysts, Studies in surface science and catalysis, vol. 96, Elsevier, 1995, pp. 829–839, https://doi.org/10.1016/S0167-2991(06)81478-3.